machines

MDPI

Article

Research on Parameter Design and Control Method for Current Source Inverter–Fed IM Drive Systems

Pengyun Song, Yanghui Liu and Chao Liu *

College of Electronical Engineering, Southwest Minzu University, Chengdu 610225, China
* Correspondence: 202031006203@stu.swun.edu.cn

Abstract: In the current source inverter (CSI)-fed inductor motor (IM) drive system, DC-bus inductance and AC-filter capacitance have a direct impact on the dynamic response speed, power quality and power density. In addition, due to the addition of filter capacitors, the mathematical model formed by the IM and capacitor is a third-order system, which increases the difficulty of parameter tuning for the control loop. To solve the above problems in the CSI, a DC-bus inductance design method based on current response speed and the ripple of the DC-link current and an AC-filter capacitance design method based on current utilization and filtering characteristics are presented. Then, the analytical expressions between the open-loop cut-off frequency, phase margin and the PI controller parameters of the current loop and speed loop are derived. Finally, an experimental platform is established to validate the proposed method.

Keywords: inductor motor (IM); current source inverter (CSI); parameter design; tuning; control loop

Citation: Song, P.; Liu, Y.; Liu, C. Research on Parameter Design and Control Method for Current Source Inverter–Fed IM Drive Systems. *Machines* **2022**, *10*, 922. https://doi.org/10.3390/machines10100922

Academic Editors: Kan Liu and Wei Hu

Received: 18 August 2022
Accepted: 28 September 2022
Published: 10 October 2022

1. Introduction

Inverters can be divided into voltage source inverter (VSI) and current source inverter (CSI) according to the characteristics of the power supply in the DC side [1,2]. For a long time, VSI has been a research hotspot and has been widely used in various AC drive and grid-connected applications [3,4]. However, the current ripple on the DC side of VSI is large, and it can only operate under the buck mode; deadtime is needed to prevent DC power supply from passing through [5]. Compared with VSI, CSI can boost the voltage and operate without short circuit protection [6]. Due to the presence of filter capacitors on the AC side, the voltage of the stator side of the motor has good waveform quality [7], so in many work situations, CSI is more suitable than VSI [8,9].

Although the CSI has the above advantages, due to some inherent defects, the application scope of CSI in motor drive systems is restricted. Instead of a constant current source, DC-link current is generated from a DC-bus inductor with a DC voltage source, and the DC-bus inductor is charged or discharged under different switching states, so the DC-link current of traditional CSI cannot be controlled [10,11]. Meanwhile, the CSI is unable to operate under the buck mode; otherwise, the DC-link current will increase continuously [12]. To achieve the control of DC-link current and a wide range of output voltage of CSI, many novel CSI topologies are proposed. In Refs. [13,14], a PWM current source rectifier is used as the front stage to control the DC-link current, but this topology is only suitable for the occasion of AC-DC-AC. In Ref. [15], a quasi-Z-source current source converter is added into the DC side, but the difficulty of control increases greatly with the addition of too many passive components. In Ref. [11], the bypass IGBT was paralleled on the DC-link inductor through the control of the switch device. Under the buck operation, the continuous increase of the DC-link current is effectively restrained. Compared to the above topologies, in Refs. [16,17], a bidirectional DC chopper is added in the front stage of the CSI; this topology is simple and consists of only a pair of switching tubes and diodes, and the DC-link current control can be achieved under the operations of boost, buck, and

deceleration by regulating the switching state of the bidirectional DC chopper. Therefore, this paper takes the topology of CSI with bidirectional DC chopper as the research object.

In the AC side of CSI, due to the presence of filter capacitors, the mathematical model formed by the motor and capacitor is a third-order system, which increases the design difficulty of the control system of the inductor motor (IM). In recent years, the vector control technologies for the CSI-fed drive system have been studied by some scholars. In Ref. [13], the references of stator current in the d-q axis are obtained by the controllers of rotor flux and speed, respectively; then, the references of the output current of the inverter bridge in the d-q axis are calculated according to the steady state equation of the IM. However, this control strategy is more sensitive to the accuracy of the IM parameters. In Ref. [18], a small signal mathematical model of a CSI-fed permanent magnet synchronous motor is constructed through the state space averaging method; a speed control system based on duty cycle regulation is proposed, but the steady-state performance of this method is not ideal, and the stator current has obvious harmonic distortion. In Ref. [19], various decoupling methods and the active damping method are presented and compared, and a control structure of voltage inner loop and current outer loop are proposed. In addition to the method of decoupling and controlling, DC-bus inductance and AC-filter capacitance also have a direct impact on the dynamic response speed, power quality, and power density [20]; however, research on parameter design methods for DC-bus inductance and AC-filter capacitance is rarely reported.

In this paper, the design principles of DC-bus inductance and AC-filter capacitance are firstly studied. Then, to reduce the number of the control loops, a vector control technology without a voltage loop is proposed, and the analytical expressions of the control parameters are derived. Finally, under various conditions, experimental validation of the proposed method is carried out.

2. Topology and Mathematical Model

2.1. Topology of CSI-Fed IM Drive System with Bidirectional DC Chopper

To realize the decoupling control of the DC-link current and IM, a bidirectional DC chopper is added between the DC voltage source and DC-link inductor; the topology is shown in Figure 1. In the figure, u_{dc} is the DC input voltage; i_{dc} is the current of DC-link inductor L_{dc}; S_1–S_6 are six switching tubes of the inverter bridge; D_1–D_6 are the diodes connected in series with S_1–S_6; C_a, C_b and C_c are the three-phase filter capacitors in the AC side; i_{at}, i_{bt} and i_{ct} are the three-phase output currents of the inverter bridge; i_{as}, i_{bs} and i_{cs} are the stator currents of the IM; u_{as}, u_{bs} and u_{cs} are the three-phase voltages of the filter capacitors. The bidirectional DC chopper is composed of the diodes D_a, D_b and the switching tubes S_a, S_b.

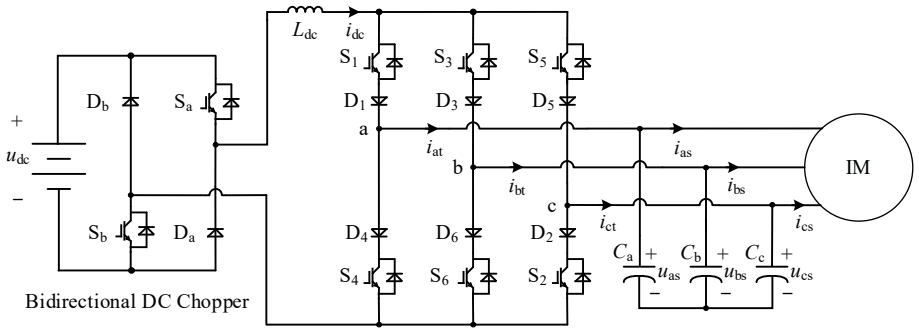

Figure 1. The topology of CSI-fed IM drive system with bidirectional DC chopper.

When the control method proposed in Ref. [17] is adopted, the circuit of DC input side can be regarded as a controlled current source. In the process of mathematical modeling and control system design for the AC side of CSI, the influence on the DC-link current can be ignored, and the topology of the CSI-fed IM drive system with bidirectional DC chopper can be simplified as seen in the circuit shown in Figure 2.

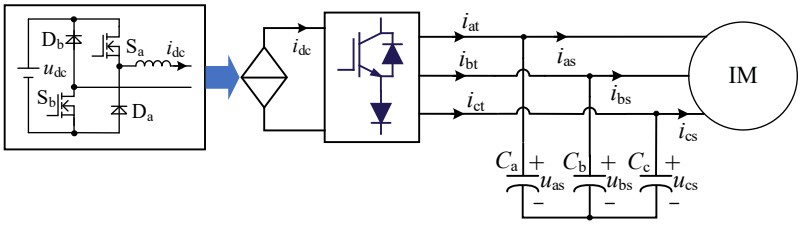

Figure 2. The equivalent circuit of CSI-fed IM drive system with bidirectional DC chopper.

2.2. Mathematical Model of Filter Capacitors and IM

In the synchronous rotating frame (d-q axis) based on rotor flux orientation, the IM voltage equation can be expressed as

$$\begin{cases} u_{ds} = \sigma L_s \frac{di_{ds}}{dt} + i_{ds} R_s - \sigma \omega_s L_s i_{qs} + \frac{L_m d\psi_r}{L_r dt} \\ u_{qs} = \sigma L_s \frac{di_{qs}}{dt} + i_{qs} R_s + \sigma \omega_s L_s i_{ds} + \omega_s \frac{L_m \psi_r}{L_r} \end{cases} \tag{1}$$

where i_{ds} and i_{qs} are the stator currents in the d-q axis; u_{ds} and u_{qs} are the voltages of filter capacitor in the d-q axis; ψ_r is the rotor flux; σ, R_s, L_m, L_r and w_s are the flux leakage coefficient, stator resistor, mutual inductance, rotor inductance and synchronous angular frequency, respectively.

According to Figure 2, the current equation in three-phase stationary coordinate frame can be expressed as

$$\begin{cases} C \frac{du_{as}}{dt} = i_{at} - i_{as} \\ C \frac{du_{bs}}{dt} = i_{bt} - i_{bs} \\ C \frac{du_{cs}}{dt} = i_{ct} - i_{cs} \end{cases} \tag{2}$$

where C represents the value of filter capacitors. Clarke transform and Park transform are carried out on Formula (3); in turn, the current equation in the d-q axis can be obtained and expressed as

$$\begin{cases} C \frac{du_{ds}}{dt} = i_{dt} - i_{ds} + \omega_s C u_{qs} \\ C \frac{du_{qs}}{dt} = i_{qt} - i_{qs} - \omega_s C u_{ds} \end{cases} \tag{3}$$

where i_{dt} and i_{qt} are the output current of the inverter bridge in the d-q axis. The rotor flux equation in the d-q axis is expressed as

$$T_r \frac{d\psi_r}{dt} + \psi_r = L_m i_{ds} \tag{4}$$

where ψ_r and L_m are the rotor flux and excitation inductor of IM, respectively, and T_r is the rotor time constant. The equations of torque and speed are expressed as

$$\begin{cases} T_e = n_p \frac{L_m}{L_r} \psi_r i_{qs} \\ J \frac{d\omega_r}{dt} = T_e - T_L \end{cases} \tag{5}$$

where J is the moment of inertia, ω_r is the mechanical speed, and T_e and T_L are the electromagnetic torque and load torque, respectively.

In summary, the mathematical model of filter capacitors and IM in the AC side of CSI can be represented by Equation (1) to Equation (5).

3. Parameter Design of DC-Link Inductance and AC-Filter Capacitance

3.1. Selection Range of DC-Link Inductance

A strong output impedance and constant current source characteristics of the DC side in CSI can be obtained by a larger DC-link inductance. However, the current regulation becomes slower as the inductance increases, which leads to overmodulation and generates

low-order current harmonics. Therefore, it is necessary to determine a selection range of DC-link inductance.

In the start-up stage, the DC-link current is too low to provide the required current for the IM, so the zero switching state is adopted, and L_{dc} is charged by u_{dc}; the equivalent circuit is shown in Figure 3a. The state equation of i_{dc} is expressed as

$$L_{dc}\frac{di_{dc}}{dt} = u_{dc} \tag{6}$$

where T_{up_max} is the maximum allowable charging time, making sure that the charging time for i_{dc} to increase from zero state to maximum DC-link current i_{dc_max} is less than T_{up_max}. L_{dc} should satisfy the following condition:

$$L_{dc} < \frac{u_{dc}T_{up\_max}}{i_{dc\_max}} \tag{7}$$

According to the conclusion in Ref. [21], the current fluctuation Δi_{dc} can be calculated when the IM is powered independently by L_{dc}, which contains two active switching states in one carried period. For example, in sector I, the equivalent discharge circuits are shown in Figure 3b,c, and Δi_{dc} is expressed as

$$\Delta i_{dc} = \frac{3T_s UI\cos\theta}{2L_{dc}i_{dc}} \tag{8}$$

where T_s is the carried period, equal to 100 μs; U is the fundamental amplitude of the stator voltage; I is the fundamental amplitude of the stator current; θ is the phase deviation between stator voltage and stator current. In other sectors, the voltage of L_{dc} and the switching state are shown in Table 1, and the expression of Δi_{dc} is consistent with that of sector I, as shown in Equation (8). Making sure that Δi_{dc} is less than the maximum ripple Δi_{dc_max} under $\theta = 1$, L_{dc} should satisfy the follow condition:

$$L_{dc} > \frac{3m_{imax}m_{umax}T_s u_{dc}}{2\Delta i_{dc\_max}} \tag{9}$$

where m_{imax} and m_{umax} are the maximum modulation ratio and boost ratio of CSI, respectively. Combining Equations (7) and (9), the selection range of L_{dc} is expressed as

$$L_{dc} \in \left(\frac{3m_{imax}m_{umax}T_s u_{dc}}{2\Delta i_{dc\_max}}, \frac{u_{dc}T_{up\_max}}{i_{dc\_max}}\right) \tag{10}$$

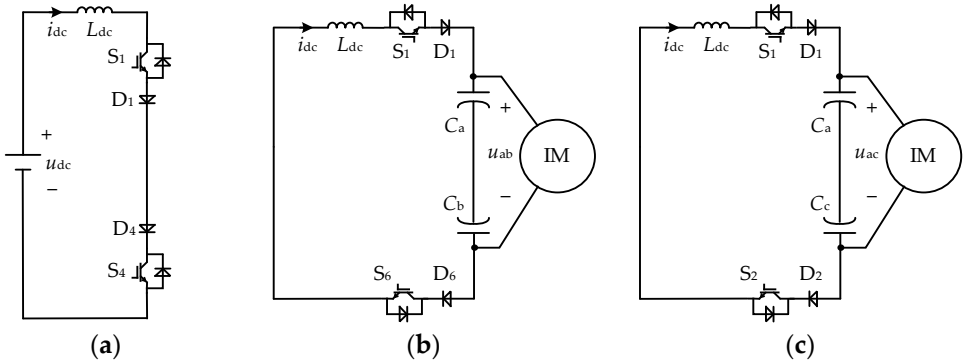

Figure 3. The equivalent circuits of charging and discharging for L_{dc}. (**a**) Equivalent charging circuit; (**b**) equivalent discharging circuit when S_1 and S_6 are turned on; (**c**) equivalent discharging circuit when S_1 and S_2 are turned on.

Table 1. The voltage of L_{dc} and switching state in sectors II–VI.

Sector	On-State Switch	Voltage of L_{dc}
II (active vector 1)	S_1 and S_2	u_{ac}
II (active vector 2)	S_2 and S_3	u_{bc}
III (active vector 1)	S_2 and S_3	u_{bc}
III (active vector 2)	S_3 and S_4	u_{ba}
IV (active vector 1)	S_3 and S_4	u_{ba}
IV (active vector 2)	S_4 and S_5	u_{ca}
V (active vector 1)	S_4 and S_5	u_{ca}
V (active vector 2)	S_5 and S_6	u_{cb}
VI (active vector 1)	S_5 and S_6	u_{cb}
VI (active vector 2)	S_6 and S_1	u_{ab}

The parameters are set as follows: $m_{imax} = 1$, $m_{umax} = 1$, $u_{dc} = 24$ V, $\Delta i_{dc\_max} = 1$ A, $i_{dc\_max} = 50$ A and $T_{up\_max} = 20$ ms. Substituting the above parameters into Equation (10), the minimum value and maximum value of DC-bus inductance are 3.6 mH and 9.6 mH, respectively.

3.2. Selection Range of AC-Filter Capacitance

The IM is represented by the T-type equivalent circuit; the phase-a circuit model of IM and the capacitor is shown in Figure 4, where $L_{s\sigma}$ and $L_{r\sigma}$ are the stator leakage inductor and rotor leakage inductor, respectively; R_r is the rotor resistor; I_{ac} is the current vector of C_a; and s_r is the slip ratio.

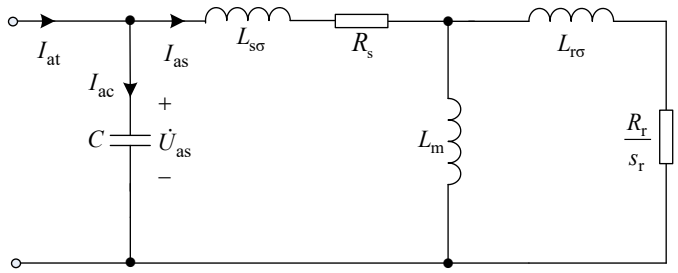

Figure 4. T-type equivalent circuit of IM with filter capacitor.

The vector diagram composed of I_{at}, I_{as}, I_{ac} and U_{as} is shown in Figure 5, and the following relationship can be obtained:

$$I_{at} = I_{ac} + I_{at} = j\omega_s C U_{as} + I_{as} \tag{11}$$

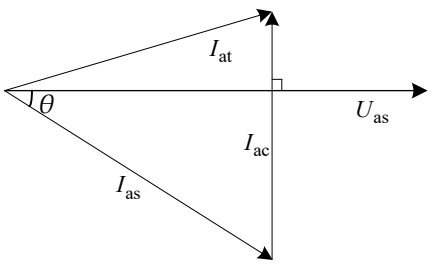

Figure 5. The vector diagram.

In order to maximize the AC current utilization rate, the following equation should be satisfied:

$$I_{at} \leq I_{as} \tag{12}$$

According to the geometric relationship in Figure 5, I_{ac} should be satisfied as follows:

$$I_{ac} \leq I_{as} \sin\theta \tag{13}$$

Substituting Equation (11) into Equation (13), the expression of maximum capacitance C_{max} can be obtained as

$$C \leq C_{max} = \frac{2I_{as} \sin\theta}{\omega_s U_{as}} \tag{14}$$

The mathematical relationship of U_{as}, I_{as} and $\sin\theta$ can be obtained according to the T-type equivalent circuit of IM shown in Figure 4, and Equation (14) can be rewritten as

$$C \leq C_{max} = \frac{2(\omega_s L_{s\sigma} + A/B)}{\omega_s \sqrt{(R_s + A/B)^2 + (\omega_s L_{s\sigma} + D/B)^2}} \tag{15}$$

where the specific forms of A, B and D are expressed as

$$\begin{cases} A &= \left(\frac{R_r R_m}{s_r} - \omega_s^2 \sigma L_r L_m\right)\left(\frac{R_r}{s_r} + R_m\right) \\ &\quad + \left(\frac{R_r \omega_s L_m}{s_r} + R_m \omega_s \sigma L_r\right)(\omega_s \sigma L_r + \omega_s L_m) \\ B &= \left(\frac{R_r}{s_r} + R_m\right)^2 + (\omega_s \sigma L_r + \omega_s L_m)^2 \\ D &= \left(\frac{R_r \omega_s L_m}{s_r} + R_m \omega_s \sigma L_r\right)\left(\frac{R_r}{s_r} + R_m\right) \\ &\quad - \left(\frac{R_r R_m}{s_r} - \omega_s^2 \sigma L_r L_m\right)(\omega_s \sigma L_r + \omega_s L_m) \end{cases} \tag{16}$$

From Equations (15) and (16), C_{max} is a function of s_r, and ω_s is set as the rated angular frequency of 100π rad/s. Substituting the IM parameters listed in Table 2 into Equations (14) and (15), the relationship curve between C_{max} and s_r can be obtained, which is shown in Figure 6. It is obvious that a minimum value occurs in C_{max}, so the AC-filter capacitance should be less than 2.37 mF.

Table 2. The parameters of the IM.

Parameters	Description	Value
R_s (Ω)	Stator resistance	0.07
R_r (Ω)	Rotor resistance	0.05
L_s (mH)	Stator inductance	4.51
L_r (mH)	Rotor inductance	4.63
L_m (mH)	Mutual inductance	4.38
σ	Flux leakage coefficient	0.088
P_n (kW)	Rated power	1.2
U_n (V)	Rated voltage	48
f_n (Hz)	Rated frequency	50
J (kg·m^2)	Rotational inertia	0.001
n_p	Number of pole pairs	2
R_s (Ω)	Stator resistance	0.07

Next, the influence mechanism on harmonic characteristics of the stator current caused by AC-filter capacitance will be discussed. The T-type equivalent circuit of IM is a third-order system; it is difficult to derive the transfer function and mathematical relationship between the capacitance and bandwidth. Since the high-order harmonic contents near the switching frequency of i_{ds} (i_{qs}) are same as the stator currents in three-phase stationary coordinate, according to Equations (1) and (2), the equivalent circuits of the IM and AC-filter capacitor in the d-q axis based on rotor flux orientation are established, as shown in Figure 7. i_{dt} and i_{qt} are composed of a DC component and several high-order harmonics components near the switching frequency. The equivalent controlled current sources, voltage sources,

and back EMFs in Figure 7 cannot amplify or attenuate harmonics, so the suppression effect of high-order harmonics is determined by R_s, σL_s and C, and the transfer function $G_{it2is}(s)$ from i_{dt} (i_{qt}) to i_{ds} (i_{qs}) can be expressed as

$$G_{it2is}(s) = \frac{1}{\sigma L_s C s^2 + R_s C s + 1} \tag{17}$$

and the oscillation angular frequency ω_n can be expressed as

$$\omega_n = \frac{1}{\sqrt{\sigma L_s C}} \tag{18}$$

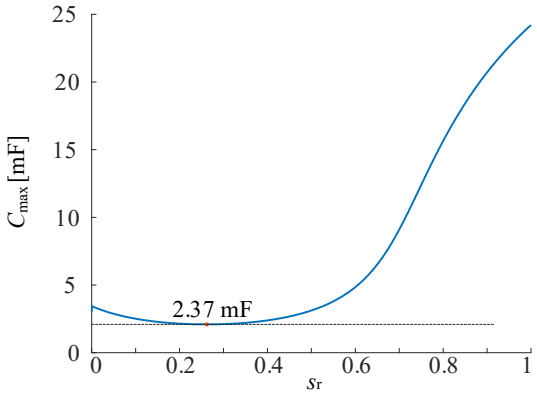

Figure 6. The relationship curve between C_{max} and s_r.

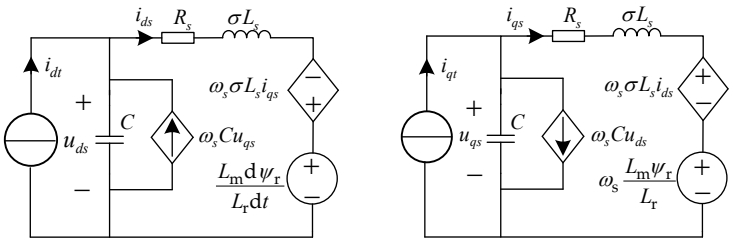

Figure 7. Second order equivalent circuit of the IM and AC-filter capacitor in the d-q axis: (**a**) d-axis; (**b**) q-axis.

Substituting the value of R_s and L_s into Equation (16), the Bode plot of $G_{it2is}(s)$ is drawn under different AC-filter capacitance, which is shown in Figure 8. It can be seen that $G_{it2is}(s)$ has a resonance spike, and the cutoff frequency decreases with the increase of C. In order to obtain the high quality stator current, $G_{it2is}(s)$ should effectively suppress the harmonic components in i_{at} near the switching frequency f_s, so the oscillation frequency should be far below f_s. This paper stipulates that the oscillation frequency is less than $f_s/2$; according to Equation (17), AC-filter capacitance should be satisfied as

$$C > \frac{1}{\sigma L_s \pi^2 f_s^2} \tag{19}$$

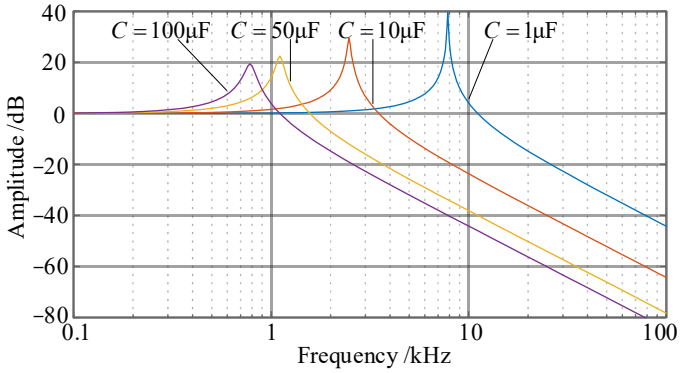

Figure 8. The Bode plot of $G_{\text{it2is}}(s)$ under different AC-filter capacitance.

Substituting the IM parameters listed in Table 2 into Equation (19), the minimum value of C is 2.5 μF.

4. Design Principle for Vector Control Strategy of CSI-Fed IM Drive System

According to Section 1, the mathematical model formed by the IM and capacitor is a third-order system; when the three closed-loop control strategy is adopted, more voltage sensors are needed, and the dynamic response to torque is slower than the VSI-fed IM drive system. In this section, a novel vector control strategy without a voltage inner loop for the CSI-fed IM drive system will be proposed, which includes current loop, flux loop and speed loop.

4.1. Analysis and Parameter Design for Current Loop

The switching delay and digital control delay are equivalent to a first-order transfer function, which is expressed as

$$G_{\text{d}}(s) = \frac{1}{1 + T_{\text{s}}s} \tag{20}$$

Due to the presence of high-frequency noise in the stator current sampling signal, a filter circuit is adopted in this paper, and its equivalent transfer function is

$$G_{\text{cf}}(s) = \frac{1}{1 + T_{\text{cf}}s} \tag{21}$$

where T_{cf} is the filter time constant, equal to 6×10^{-5} in this paper.

Ignoring the coupling terms in Equations (1) and (3), such as $\omega_{\text{s}}\sigma L_{\text{s}}i_{\text{qs}}$, $\omega_{\text{s}}\sigma L_{\text{s}}i_{\text{ds}}$, $\omega_{\text{s}}Cu_{\text{qs}}$ and $\omega_{\text{s}}Cu_{\text{ds}}$, in the d-q axis, the control diagram of the current loop without stator voltage sampling and control is shown in Figure 9, where k_{cp} and τ_{ci} are the proportional coefficient and integral coefficient of PI controller for adjusting the stator current, i^*_{dt} and i^*_{qt} are the reference value of output current of the inverter bridge in the d-q axis, i^*_{ds} and i^*_{qs} are the reference value of the stator currents in the d-q axis.

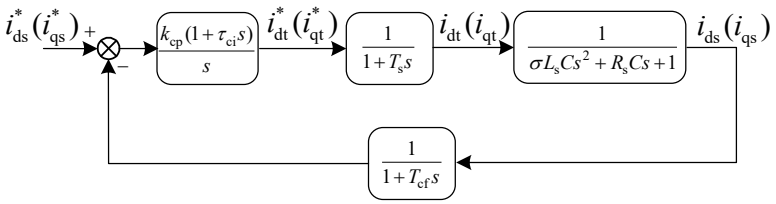

Figure 9. The control diagram of the current loop.

In this paper, the target cut-off frequency and phase margin of current loop are represented as ω_{cc} and φ_{cc}. According to Figure 9, Q_{c_amp}, the amplitude of the current open-loop at ω_{cc}, can be derived as follows:

$$Q_{c\_amp} = \sqrt{\frac{1}{[1+(T_s\omega_{cc})^2][1+(T_{cf}\omega_{cc})^2][(1-\sigma L_s C\omega_{cc}^2)^2+R_s^2C^2\omega_{cc}^2]}} \tag{22}$$

φ_{c_phase}, the phase of the current open-loop at ω_{cc}, can be derived as follows:

$$\varphi_{c\_phase} = -\arctan(T_s\omega_{cc}) - \arctan(T_{cf}\omega_{cc}) - \arctan(\frac{R_sC\omega_{cc}}{1-\sigma L_sC\omega_{cc}^2}) \tag{23}$$

To ensure that the phase angle margin of the current loop with the PI controller is greater than φ_{cc}, τ_{ci} should be satisfied as follows:

$$\tau_{ci} \geq \frac{\tan(\varphi_{cc} - \varphi_{c\_phase} - \frac{\pi}{2})}{\omega_{cc}} \tag{24}$$

To ensure that the amplitude of the current loop with the PI controller is equal to 1, k_{cp} should be satisfied as follows:

$$k_{cp} = \frac{\omega_{cc}}{Q_{c\_amp}\sqrt{1+\tau_{ci}^2\omega_{cc}^2}} \tag{25}$$

In order to achieve fast dynamic response and the effective suppression of high-order harmonics in the output current of the inverter bridge, ω_{cc} is set to 2000π rad/s, which is one-tenth of the switching frequency. Meanwhile, to obtain a better stability, φ_{cc} is set to $\pi/4$ rad. Substituting the parameters listed in Table 2 into Equation (22) to Equation (25), k_{cp} and τ_{ci} can be calculated as 0.98 and 22.15, respectively. The Bode plot of the current closed-loop transfer function $G_i(s)$ is shown in Figure 10; the bandwidth of $G_i(s)$ is 1kHz, and the amplitude remains 0 dB when the frequency is less than 1kHz. When the frequency is greater than 1 kHz, the amplitude decays with a slope close to -60 dB/dec, which can effectively suppress the high-order harmonics generated in the switching process. This explains that a good steady-state and dynamic performance can be achieved by the PI parameter optimization proposed in this paper. In order to facilitate the subsequent parameter design of the external loop control system, $G_i(s)$ is simplified to a second-order transfer function and expressed as

$$G_i(s) = \frac{3.13\times10^5}{1.65\times10^{-3}s^2+37.1s+3.13\times10^5} \tag{26}$$

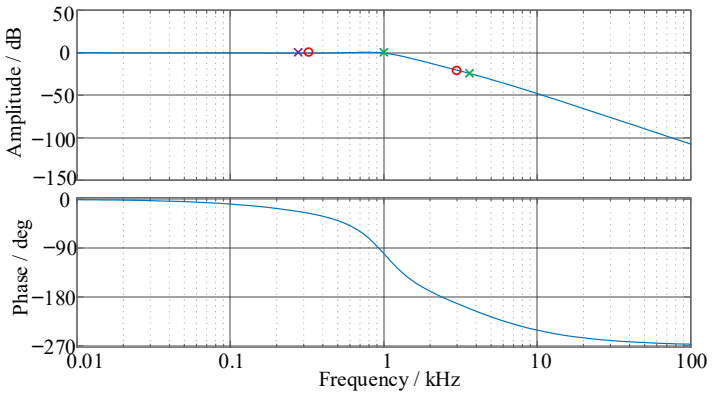

Figure 10. Bode plot of transfer function of current closed loop.

4.2. Analysis and Parameter Design for Flux Loop

A PI controller is adopted to adjust rotor flux ψ_r and is combined with Equation (4); the diagram of the flux loop with a PI controller is shown in Figure 11. $k_{\psi p}$ and $\tau_{\psi i}$ are the proportional coefficient and integral coefficient of the PI controller.

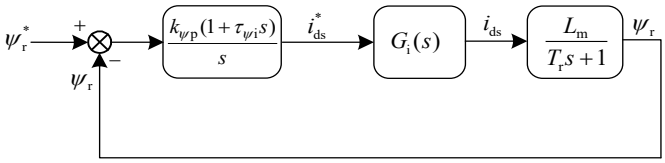

Figure 11. The control diagram of the flux loop.

To simplify the design method of the control parameters, zero-pole cancellation is adopted, and $\tau_{\psi i}$ is set to T_r. Then, the root locus plot is utilized to determine $k_{\psi p}$, which is shown in Figure 12. It is obvious that the condition for the stability of the flux loop is as follows:

$$k_{\psi P} \in (0, 6.21/L_m) \tag{27}$$

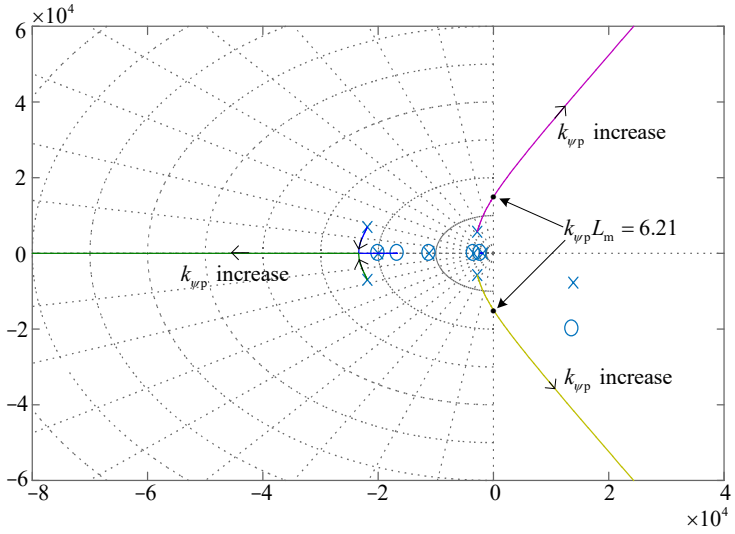

Figure 12. Root locus plot of rotor flux loop.

Finally, $k_{\psi p}$ is obtained by the Sisotool box of Matlab, where $k_{\psi p}$ is equal to $3.15/L_m$; the Bode plot of flux open-loop is shown in Figure 13. The cut-off frequency is 600 Hz, and the phase margin is 60°.

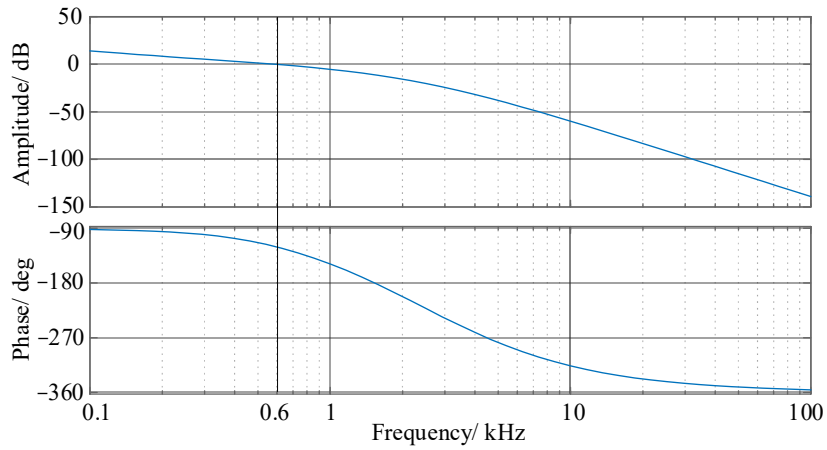

Figure 13. Bode plot of rotor flux open loop.

4.3. Analysis and Parameter Design for Speed Loop

The speed of IM is sampled by an orthogonal encoder, and the sampling frequency is half of f_s; the transfer function of speed sampling and delay is expressed as

$$G_{sf}(s) = \frac{1}{1 + 2T_s s} \tag{28}$$

In accordance with Equations (5) and (6), the block diagram of the speed loop under the PI controller is shown in Figure 14, where k_{sp} and τ_{si} are the proportional coefficient and integral coefficient of the PI controller for adjusting the stator current, respectively. ω_s^* is the rated angular frequency. It is noted that the speed loop contains variable ψ_r, so the cut-off frequency of the speed open loop should be less than that of the flux open loop, and ψ_r is set as 0.05 Wb. The open-loop transfer function of speed $G_{s\_open}(s)$ can be expressed as

$$G_{s\_open}(s) = \frac{3n_p L_m \psi_r k_{sp} G_i(s)(1 + \tau_{si})}{2JL_r s^2(1 + 2T_s s)} \tag{29}$$

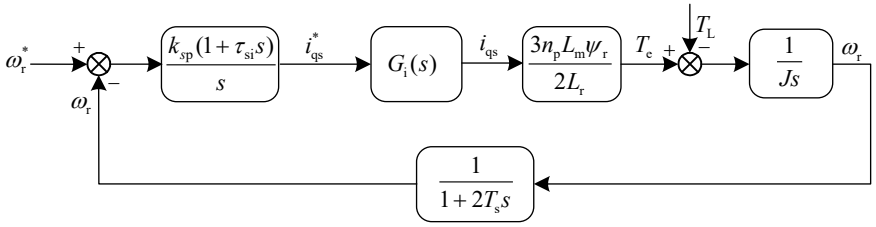

Figure 14. The control diagram of the speed loop.

The close-loop transfer function of speed $G_{s\_close}(s)$ is expressed as

$$G_{s\_close}(s) = \frac{G_{s\_open}(s)(1 + 2T_s s)}{1 + G_{s\_open}(s)} \tag{30}$$

The target cut-off frequency and phase margin of the speed loop are represented as ω_{ss} and φ_{ss}. Using the same method as the current PI controller, the analytical formulas of ω_{ss} and φ_{ss} are derived as follows:

$$\begin{cases} \tau_{si} = \frac{\tan(\varphi_{ss} - \varphi_{s\_phase} - \frac{\pi}{2})}{\omega_{ss}} \\ k_{sp} = \frac{\omega_{ss}}{Q_{s\_amp}\sqrt{1+\tau_{si}^2\omega_{ss}^2}} \end{cases} \tag{31}$$

where Q_{s_amp} and φ_{s_phase} are the amplitude and phase of the speed open loop at ω_{ss} before the PI controller, respectively. k_{sp} and τ_{si} are obtained by substituting the equation $\omega_{ss} = 200\pi$ rad/s and $\varphi_{ss} = \pi/6$ rad into Equation (31). The specific expression of $G_{s\_close}(s)$ is as follows:

$$G_{s\_close}(s) = \frac{30.89s^4 + 8.5 \times 10^5 s^3 + 9.34 \times 10^9 s^2 + 2.93 \times 10^{13} s + 2.93 \times 10^{11}}{5.425 \times 10^{-10} s^7 + 2.716 \times 10^{-5} s^6 + 0.6 s^5 + 7045 s^4 + 4.29 \times 10^7 s^3 + 1.01 \times 10^{11} s^2 + 2.93 \times 10^{13} s + 2.93 \times 10^{11}} \tag{32}$$

The Bode plots of open-loop and closed-loop transfer functions are shown in Figure 15. The cut-off frequency of the speed open-loop transfer function is 100 Hz, and the phase margin is 30°. The closed-loop transfer function has a good following characteristic in the bandwidth of 40 Hz. The unit step response of the speed closed-loop transfer function is shown in Figure 16; the rise time is only 2 ms, the overshoot is little, and no steady-state error occurs.

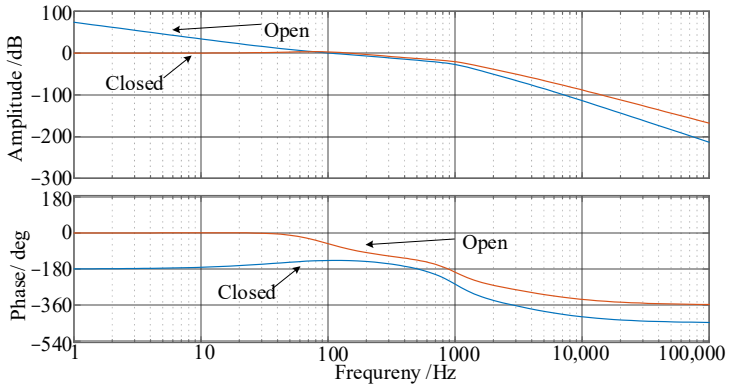

Figure 15. Bode plot of speed open loop and closed loop.

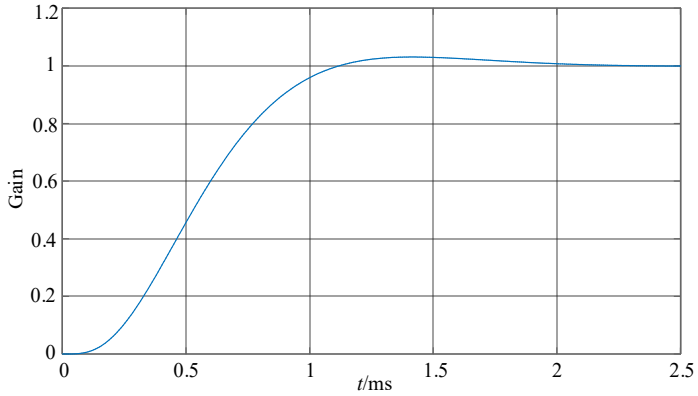

Figure 16. Step response plot of speed closed loop.

5. Simulation Results

The simulation model of the CSI-fed IM drive system with bidirectional DC chopper is built on MATLAB Simulink, including the power module, control module and modulation module. The parameters of IM adopted are consistent with Table 2, and other simulation parameters are shown in Table 3.

Table 3. Simulation parameters.

Parameters	Value
DC-link inductor L_{dc}	4 mH
Filter capacitor C_a, C_b, C_c	66 μF
DC-bus voltage u_{dc}	20 V
Switching frequency	10 kHz
Sampling frequency	10 kHz

5.1. Load Acceleration Condition

The value of load torque is set to 3 N·m, the initial reference speed is 1500 rpm, and the reference speed is 3000 rpm when the time is 0.8 s. The simulation waveforms of stator phase a current, stator currents in the d-q axis, electromagnetic torque, motor speed and rotor flux in the whole simulation process are shown in Figure 17.

To improve DC-link current utilization and reduce losses and harmonic distortion, according to the MTPA method proposed in Ref. [17], the references of rotor flux and DC-link current are adjusted with the change of operating point; the specific principle is as follows:

A. In the dynamic process, in order to provide greater torque, the reference DC-link current is set to 50 A, which is the maximum current of the DC-link inductor.

B. In the steady state, the references of rotor flux ψ_r^* and DC-link current i_{dc}^* are adjusted according to the load torque and speed, which are shown in Table 4.

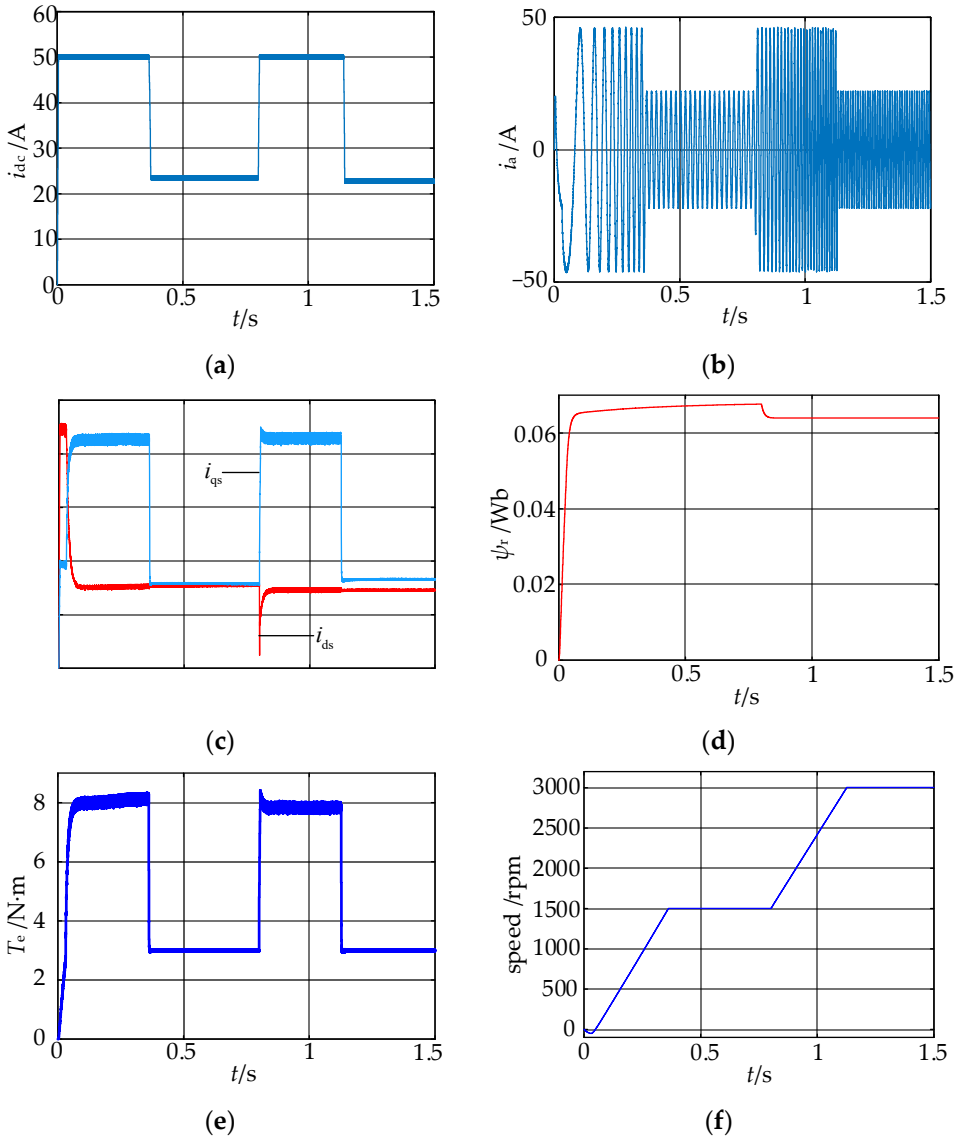

Figure 17. Simulation waveform under load torque of 3 N·m. (**a**) i_{dc}; (**b**) i_a; (**c**) i_d and i_q; (**d**) ψ_r; (**e**) T_e; (**f**) Speed.

Table 4. The reference of rotor flux and DC-link current under different load torque.

T_e (N·m)	Speed (rpm)	ψ_r^* (Wb)	i_{dc}^* (A)
0	1500	0.03	11.5
0	900	0.031	12
1	1500	0.039	14.8
2	1500	0.055	20.9
3	1500	0.068	23.5
3	3000	0.064	22.8

The whole simulation process is divided into three stages.

Start-up stage: in order to make the motor speed reach the reference speed as soon as possible, the hysteresis control strategy of DC-link current is adopted to regulate i_{dc} to 50 A, which is the max reference, so as to meet the demand of current. The optimal reference

value of rotor flux ψ_r^* is 0.068 Wb. After 0.05 s, ψ_r^* reaches the reference value, i_{ds} is around 15 A, i_{qs} is around 43 A, and T_e is 8 N·m. After 0.4 s, the speed is adjusted to 1500 rpm, and T_e is reduced to 3 N·m.

Steady-state operation stage at 1500 rpm: i_{dc} is regulated to 23.5 A, as shown in Figure 17a. It can be seen from Figure 17e that when i_{dc} is reduced to 23.5 A, the ripple of torque is significantly reduced.

Second acceleration stage: at the time of 0.8 s, the value of step speed is 3000 rpm. i_{dc} reach to 50 A again, which is the same as the start-up stage. When ψ_r^* is adjusted to 0.064 Wb, i_{ds} is reduced immediately, ψ_r follows the given value quickly, i_{qs} and T_e are the same as the start-up. Finally, at 1.08 s, the speed reaches to 3000 rpm.

5.2. Deceleration Condition with No Load

This section simulates the deceleration condition of the motor with no load. When the IM speed reaches the rated speed of 1500 rpm, the reference speed is changed to 900 rpm at 0.6 s. The simulation waveforms of electromagnetic torque, speed, DC-link current and output power of DC power supply are shown in Figure 18, respectively. When the speed decelerates, i_{dc} is around 30 A. The electromagnetic torque plays a braking role and reaches to −2.3 N·m, and the speed reaches stability again after 0.28 s. The DC power supply intermittently absorbs the energy feedback from the motor decelerating process, and the output power is less than zero, so the energy feedback is realized.

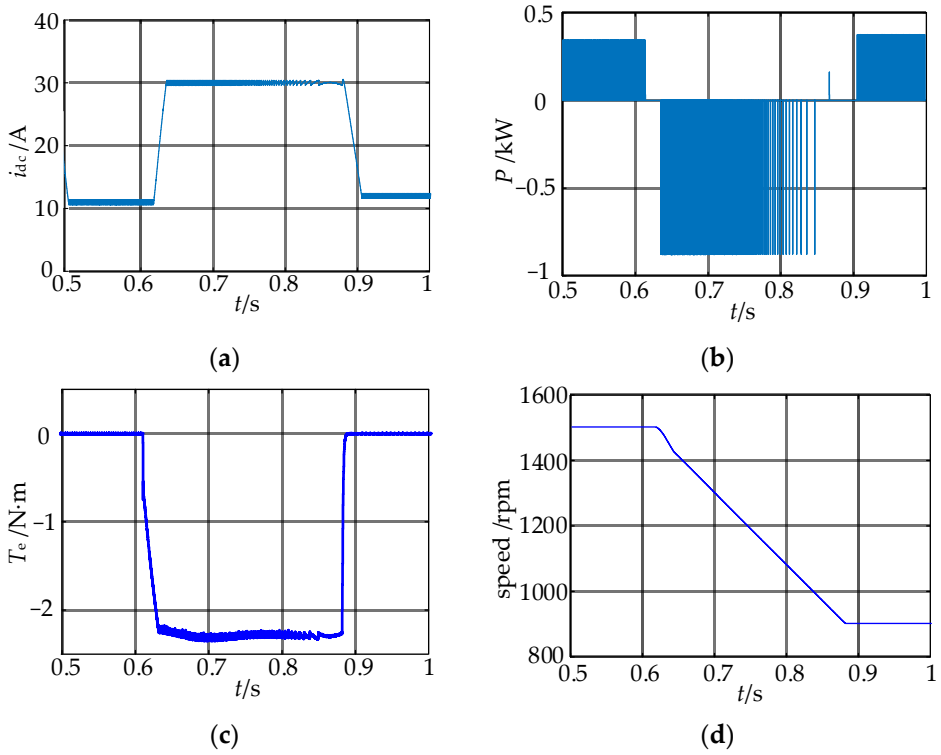

Figure 18. Simulation waveform under no-load deceleration. (**a**) i_{dc}; (**b**) output power of DC power supply; (**c**) T_e; (**d**) speed.

5.3. Load Disturbance Condition

Figure 19 are the simulation waveforms of load disturbance, when the speed remains at 1500 rpm, the load torque is reduced from 3 N·m to 1 N·m at 0.1 s, and the speed controller makes the electromagnetic torque drop rapidly to 1 N·m, where the speed remains unchanged. At the same time, the ψ_r and i_{dc} are reduced to the optimal value of 0.039 Wb and the minimum value of 14.8 A, respectively. When the load torque is increased to 2 N·m at 0.3 s, the speed is stabilized at 1500 rpm after 0.16 s, and the maximum error of speed is only 14 rpm. The ψ_r and i_{dc} are adjusted to 0.055 Wb and 20.9 A, respectively.

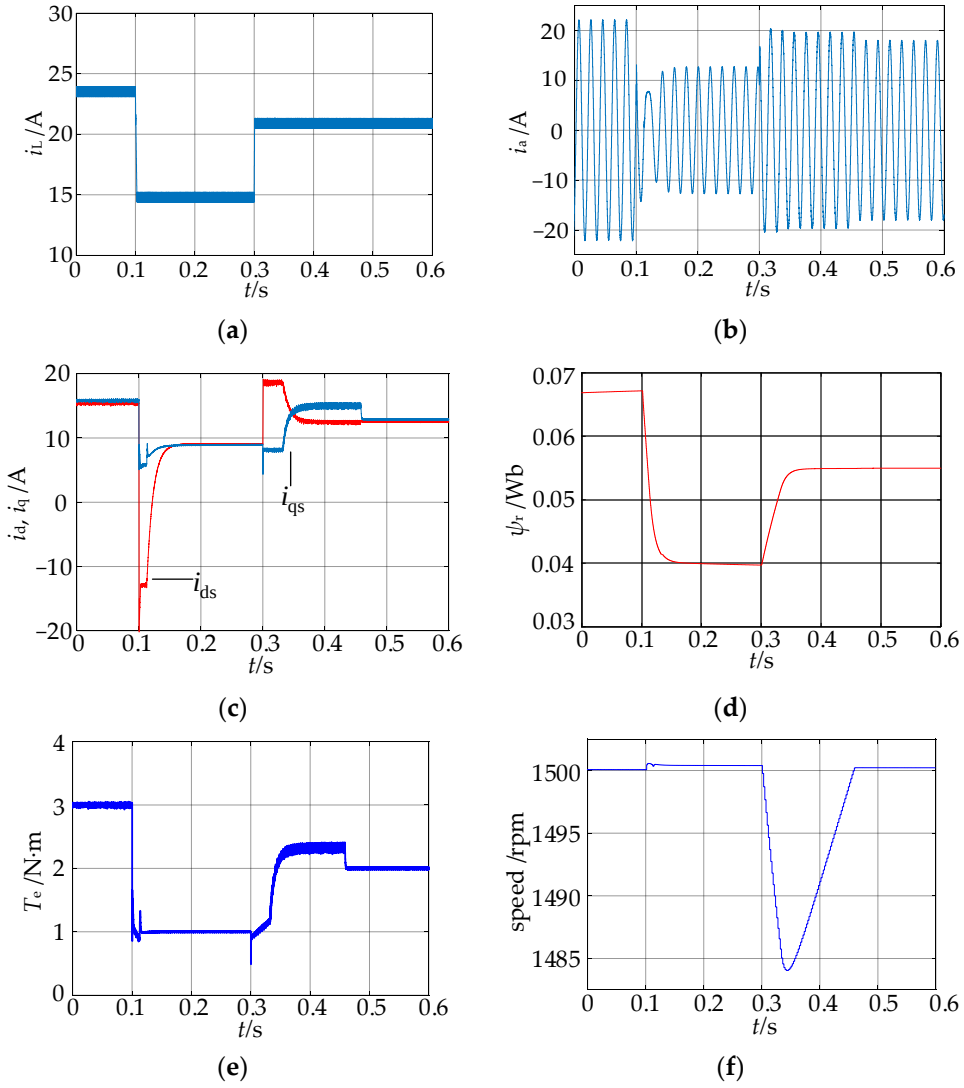

Figure 19. Simulation waveforms under the step perturbation of load torque. (**a**) i_L; (**b**) i_a; (**c**) i_d and i_q; (**d**) ψ_r; (**e**) T_e; (**f**) speed.

6. Experimental Results

In order to verify the feasibility of parameter design for DC-link inductance and AC-filter capacitance and the effectiveness of the vector control strategy proposed in this paper, the experimental platform was established, as shown in Figure 20; the experimental parameters are shown in Table 5. The value of DC-link inductance and AC-filter capacitance are satisfied with the selection range specified in Section 3. Because the motor speed, rotor flux, and stator d-q axis current cannot be measured by the oscilloscope, in order to facilitate debugging as well as the observation and storage of these signals, this paper develops a host computer program on the GUI platform of MATLAB to realize the data communication with DSP.

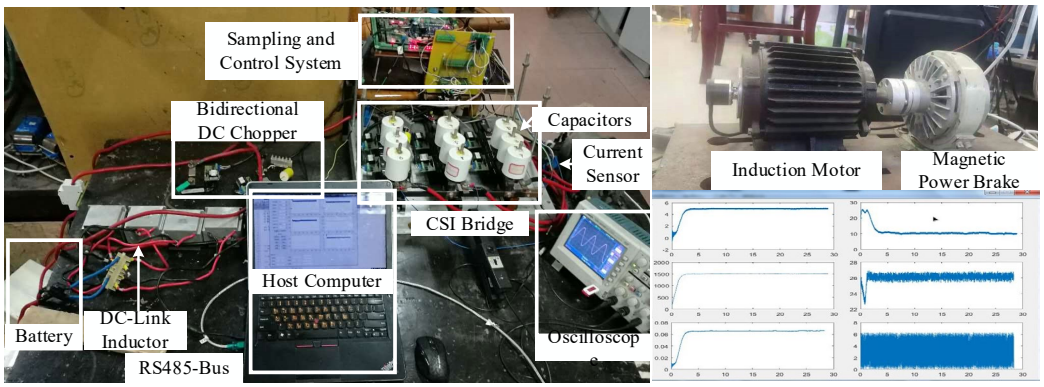

Figure 20. Prototype for CSI-fed IM drive system with bidirectional DC chopper.

Table 5. Models and parameters of the experimental platform.

Category	Part Number	Parameters
DC-link inductor L_{dc}	custom-made	4 mH
Filter capacitor C_a, C_b, C_c	MKP1847610354P4	66 μF
DC-bus voltage u_{dc}	Battery	24 V
Current sensors	LEM LA28-P	/
Diode modules	RM300HA-24F	240 V/300 A
IGBT modules	PM400HSA120	400 V/120 A
DSP	TMS320F28335	/
Encoder	OIH, 2500C/T	/

Next, the experimental results will be carried out under the three operation conditions: acceleration with load, deceleration with no-load and change of load.

6.1. Performance under Acceleration with Load of 3 N·m

Experimental waveforms of accelerated conditions are shown in Figure 21, under the load of 3 N·m. The experimental process consists of two stages. The reference speed changes from 1500 rpm to 3000 rpm, in order to reduce the harmonics and losses, and to improve current utilization, the references of i_{dc} and ψ_r are also adjusted according to the calculation method for the minimum DC-link current and the optimal flux proposed in Ref. [17]. In the dynamic process, to obtain a larger torque and reduce the dynamic response time, the reference i_{dc} is set to 50 A. In the first stage, the reference speed is set to 1500 rpm, and the reference i_{dc} and ψ_r are set to 23.5 A and 0.068 Wb, respectively. In the second stage, the reference speed is set to 3000 rpm, and the reference i_{dc} and ψ_r are set to 22.5 A and 0.065 Wb, respectively. From Figure 21, the rise time of i_{dc} increasing from 0 A to 50 A is only 15 ms, and the ripple of i_{dc} is less than 0.5 A, which demonstrates that the parameter design method of the DC-link inductor is feasible. In two stages, the speed and rotor flux can quickly track the references, and the THD of the stator current is less than 2%.

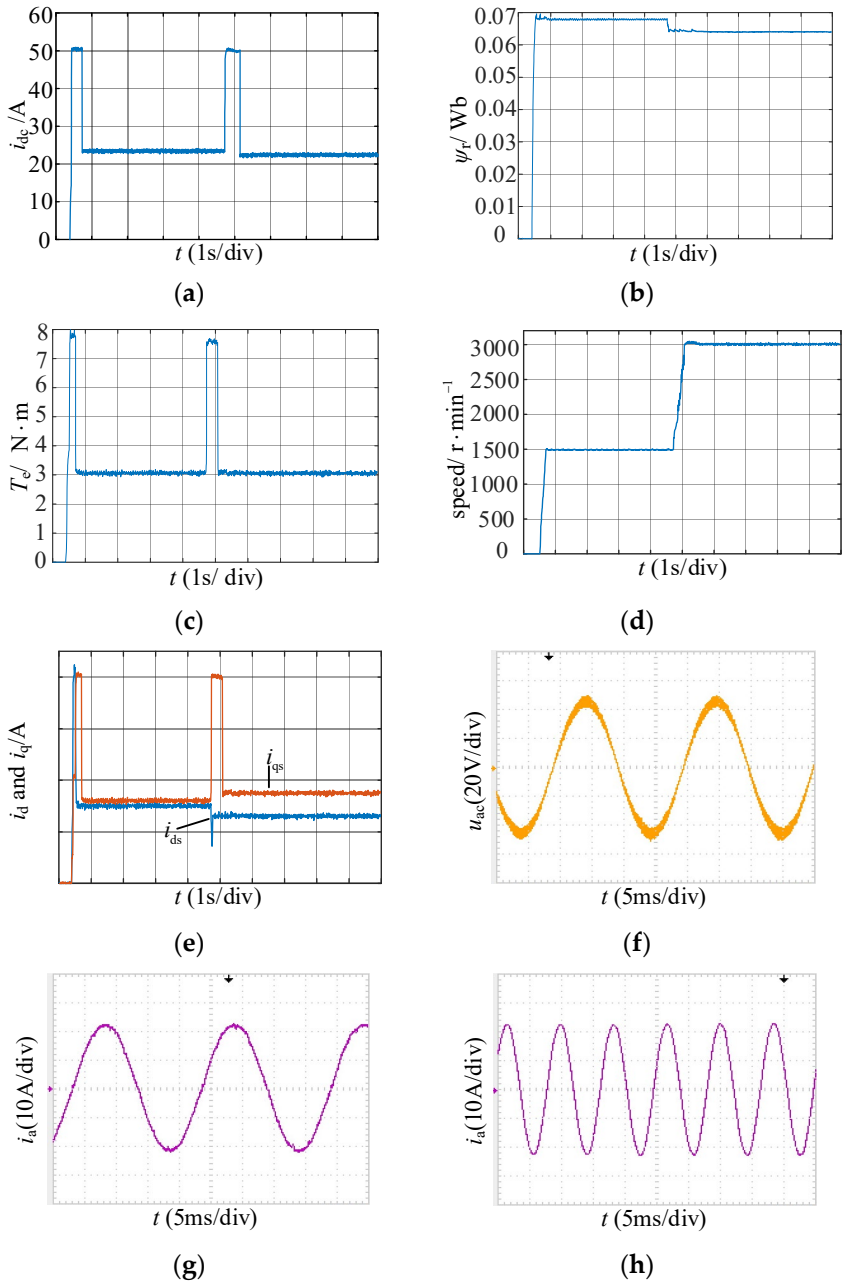

Figure 21. Experimental waveforms under acceleration with load of 3 N·m: (**a**) DC-link current; (**b**) Rotor flux; (**c**) Torque; (**d**) Speed; (**e**) Stator current in d-q axis; (**f**) Stator voltage of phase-a; (**g**) Stator current of phase-a under speed of 1500 rpm; (**h**) Stator current of phase-a under speed of 3000 rpm.

6.2. Performance under Deceleration with No Load

The experimental waveforms of the reference speed decreasing from 1500 rpm to 900 rpm with no load are shown in Figure 22. Unlike with the operational condition where the load is 3 N·m, the amplitude of the stator voltage is 18.5 V, which is less than u_{dc}. i_{dc} remains at 12 A with little ripple in the steady state, and during the dynamic process of speed decreasing from 1500 rpm to 900 rpm, the reference of i_{dc} is set to 30 A, and the mechanical energy from IM is recovered by the DC voltage source. Due to a fast dynamic and little ripple of T_e, dynamic and steady performance of speed can be obtained, the rotor flux can quickly track the references, and the stator current has very little harmonic distortion.

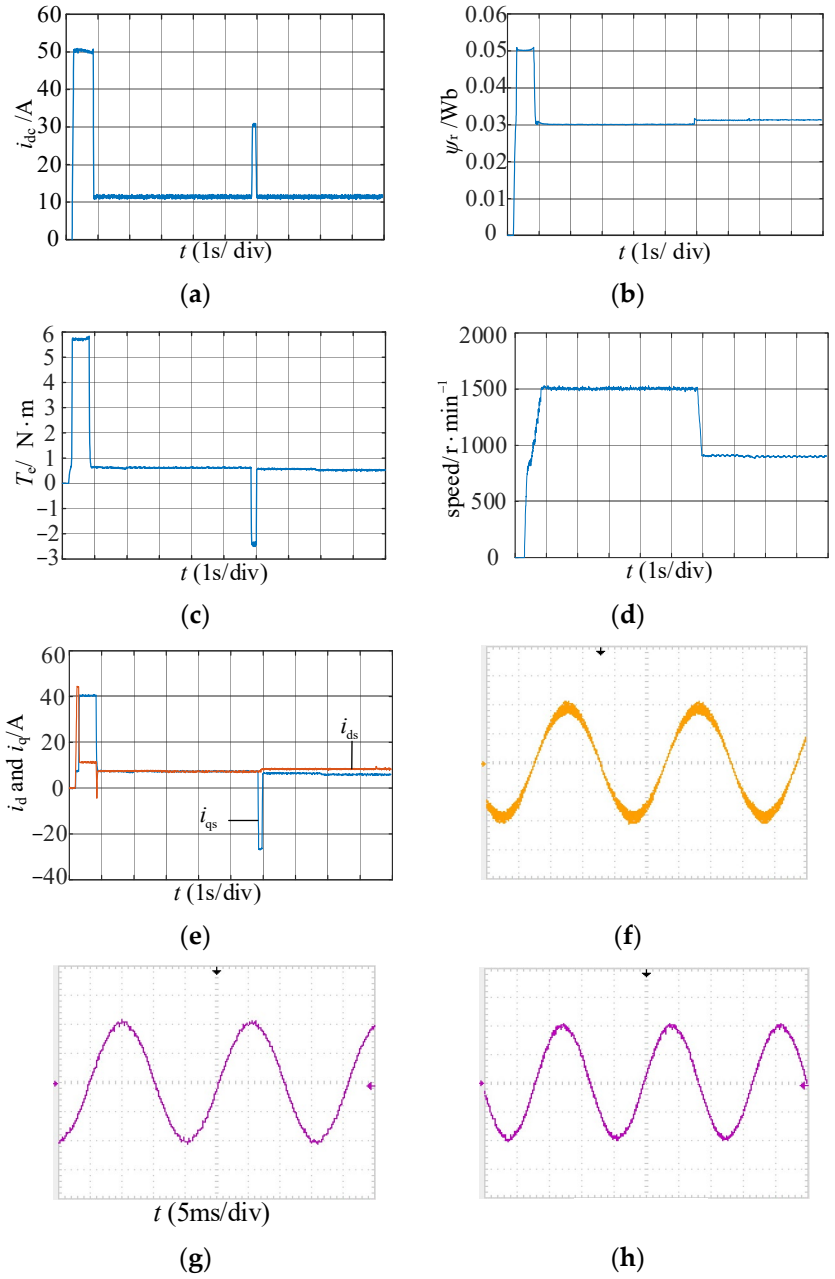

Figure 22. Experimental waveforms under deceleration with no load: (**a**) DC-link current; (**b**) Rotor flux; (**c**) Torque; (**d**) Speed; (**e**) Stator current in d-q axis; (**f**) Stator voltage of phase-a under speed of 900 rpm; (**g**) Stator current of phase-a under speed of 1500 rpm; (**h**) Stator current of phase-a under speed of 900 rpm.

6.3. Performance under Different Loads

The reference speed is set to 1500 rpm. The IM starts with the load of 3 N·m, then the load is suddenly reduced to 1 N·m, and finally the load is increased to 2 N·m. The experimental waveforms are shown for the reference speed decreasing from 1500 rpm to 900 rpm with no load are shown in Figure 23. Since the torque can be quickly adjusted when the sudden change occurs on the load, the fluctuation of the speed is less than 3%. Meanwhile, i_{dc} and ψ_r can quickly track the references.

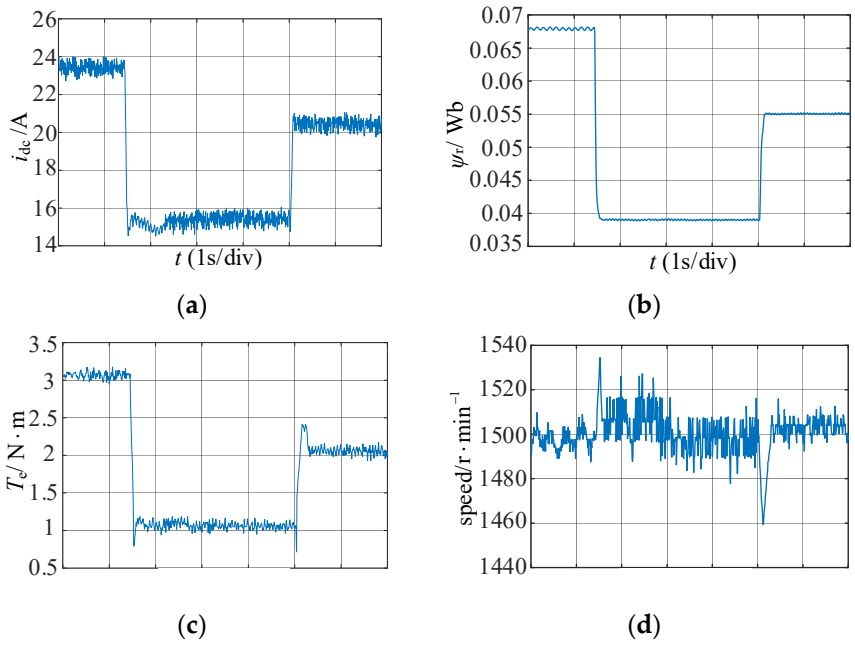

Figure 23. Experimental waveforms under different loads: (**a**) DC-link current; (**b**) Rotor flux; (**c**) Torque; (**d**) Speed.

7. Conclusions

In order to improve the performance of the current source inverter–fed inductor motor drive system, this paper presents a novel design principle of DC-bus inductance and AC-filter capacitance, and a vector control technology without voltage loop. The feasibility and correctness are verified by the simulation and experimental results under various operating conditions. The main contributions can be summarized as follows:

(1) Under consideration of the dynamic response speed and current ripple, the range expression of the DC-link inductance is derived.
(2) Under consideration of the DC-link current utilization and harmonic suppression, the range expression of the AC-filter inductance is derived.
(3) The simulation and experimental results show that the fast dynamic performance of speed and flux with no overshoot and a stator current with low harmonic distortion can be obtained by the vector control strategy without voltage loop for current source inverter–fed inductor motor drive systems. The analytical expressions of the control parameters derived in this paper are also suitable for other IM parameters.

Author Contributions: Conceptualization and methodology, P.S.; simulation, Y.L.; validation and experiment, P.S. and C.L.; writing and supervision, P.S.; review and editing, C.L. funding acquisition, P.S. All authors have read and agreed to the published version of the manuscript.

Funding: This work was supported in part by the Southwest Petroleum University City-School Cooperation Strategic Project under Grant 18SXHZ0043.

Data Availability Statement: Not applicable.

Conflicts of Interest: The authors declare that there is no conflict of interest regarding the publication of this paper.

References

1. Lorenzani, E.; Migliazza, G.; Immovilli, F.; Buticchi, G. CSI and CSI7 current source inverters for modular transformerless PV inverters. *Chin. J. Electr. Eng.* **2019**, *5*, 32–42. [CrossRef]
2. Wang, W.; Gao, F.; Yang, Y. An eight-switch five-level current source inverter. *IEEE Trans. Power Electron.* **2018**, *34*, 8389–8404. [CrossRef]

3. Zhou, S.; Liu, K.; Hu, W.; Chen, Y.; Zhang, D.; Huang, Q.; Tong, Q.; Zhang, Q. Harmonic-Separation-Based Direct Extraction and Compensation of Inverter Nonlinearity for State Observation Control of PMSM. *IEEE Access* **2021**, *9*, 142028–142045. [CrossRef]
4. Dong, Z.; Liu, C.; Song, Z.; Liu, S. Suppression of Dual-Harmonic Components for Five-Phase Series-Winding PMSM. *IEEE Trans. Transp. Electrif.* **2022**, *8*, 121–134. [CrossRef]
5. Zhao, L.; Chen, Z.; Wang, H.; Li, L.; Mao, X.; Li, Z.; Zhang, J.; Wu, D. An Improved Deadbeat Current Controller of PMSM Based on Bilinear Discretization. *Machines* **2022**, *10*, 79. [CrossRef]
6. Zhao, J.; Lu, H. Study on a new control strategy based on three phase current inverter. In Proceedings of the 2017 Eighth International Conference on Intelligent Control and Information Processing (ICICIP), Hangzhou, China, 3–5 November 2017; pp. 151–156.
7. Rajeev, M.; Agarwal, V. Single phase current source inverter with multiloop control for transformerless grid—PV interface. *IEEE Trans. Ind. Appl.* **2018**, *54*, 2416–2424. [CrossRef]
8. Chen, D.; Jiang, J.; Qiu, Y.; Zhang, J.; Huang, F. Single-stage three-phase current-source photovoltaic grid-connected inverter high voltage transmission ratio. *IEEE Trans. Power Electron.* **2016**, *32*, 7591–7601. [CrossRef]
9. Xing, L.; Wei, Q. Series-connected current source inverters with less switches. *IEEE Trans. Power Electron.* **2019**, *35*, 5553–5556. [CrossRef]
10. Xu, Y.; Wang, Z.; Liu, P.; Wu, J.; Cheng, M. A new control method for current-source inverter fed motor drive system without additional DC-link current regulator. In Proceedings of the 2020 IEEE 9th International Power Electronics and Motion Control Conference (IPEMC2020-ECCE Asia), Nanjing, China, 29 November–2 December 2020; pp. 382–387.
11. Miao, Y.; Liu, H.; Wang, H.; Wang, M. The modulation and control strategy of storage inductance current for single-phase current source inverter. *Trans. China Electrotech. Soc.* **2018**, *33*, 1227–1237.
12. Wang, W.; Gao, F.; Yang, Y.; Blaabjerg, F. Operation and modulation of H7 current-source inverter with hybrid SiC and Si semiconductor switches. *IEEE J. Emerg. Sel. Top. Power Electron.* **2017**, *6*, 387–399. [CrossRef]
13. Li, Y.W.; Pande, M.; Zargari, N.R.; Wu, B. DC-link current minimization for high-power current-source motor drives. *IEEE Trans. Power Electron.* **2008**, *24*, 232–240.
14. Ding, L.; Li, Y.W.; Zargari, N.R. Discrete-time SMO sensorless control of current source converter-fed PMSM drives with low switching frequency. *IEEE Trans. Ind. Electron.* **2020**, *68*, 2120–2129. [CrossRef]
15. Yang, S.; Peng, F.Z.; Lei, Q.; Inoshita, R.; Qian, Z. Current-fed quasi-Z-source inverter with voltage Buck–Boost and regeneration capability. *IEEE Trans. Ind. Appl.* **2010**, *47*, 882–892. [CrossRef]
16. Xu, Y.; Wang, Z.; Liu, P.; He, J. A Soft-Switching Current-Source-Inverter-Fed Motor Drive With Reduced Common-Mode Voltage. *IEEE Trans. Ind. Electron.* **2021**, *68*, 3012–3021. [CrossRef]
17. Miao, Y.; Liu, H.; Zhang, W.; Liu, P. Optimal control strategy of storage inductor current and rotor flux for current source inverter motor drive system. *Proc. CSEE* **2021**, *39*, 2757–2767.
18. Migliazza, G.; Buticchi, G.; Carfagna, E.; Lorenzani, E.; Madonna, V.; Giangrande, P.; Galea, M. DC current control for a single-stage current source inverter in motor drive application. *IEEE Trans. Power Electron.* **2021**, *36*, 3367–3376. [CrossRef]
19. Lee, H.-J.; Jung, S.; Sul, S.-K. A current controller design for current source inverter-fed AC machine drive system. *IEEE Trans. Power Electron.* **2013**, *28*, 1366–1381. [CrossRef]
20. Fuchs, F.W.; Kloenne, A. DC link and dynamic performance features of PWM IGBT current source converter induction machine drives with respect to industrial requirements. In Proceedings of the 4th International Power Electronics and Motion Control Conference (IPEMC), Xi'an, China, 14–16 August 2004; Volume 3, pp. 1393–1398.
21. Miao, Y.; Liu, H.; Hua, Z.; Liu, J.; Cheng, Z. Control strategy for three-phase current source inverter based on optimal given value of DC storage inductance current. *Trans. China Electrotech. Soc.* **2019**, *34*, 349–362.